Supporting Information for

Revealing and Modulating Catalyst Reconstruction for Highly Efficient Electrosynthesis of Ammonia

Xinyue Shi[1†], Wei-Hsiang Huang[2,3†], Ju Rong[4], Minghui Xie[1], Qingbo Wa[5], Ping Zhang[1], Hainan Wei[1], Huangyu Zhou[1], Min-Hsin Yeh[3,6], Chih-Wen Pao[2], Jie Wang[7], Zhiwei Hu[8], Xiaohua Yu[4*], Jiwei Ma[1*], Hongfei Cheng[1*]

[1]Shanghai Key Laboratory for R&D and Application of Metallic Functional Materials, Institute of New Energy for Vehicles, School of Materials Science and Engineering, Tongji University, Shanghai 201804, China.

[2]National Synchrotron Radiation Research Center, Hsinchu 300092, Taiwan.

[3]Sustainable Electrochemical Energy Development Center, National Taiwan University of Science and Technology, Taipei 106, Taiwan.

[4]Faculty of Materials Science and Engineering, Kunming University of Science and Technology, Kunming 650093, China.

[5]Department of Chemistry, City University of Hong Kong, Hong Kong, China.

[6]Department of Chemical Engineering, National Taiwan University of Science and Technology, Taipei 106, Taiwan.

[7]Key Laboratory of Fluid and Power Machinery of Ministry of Education, School of Materials Science and Engineering, Xihua University, Chengdu, Sichuan 610039, China.

[8]Max Planck Institute for Chemical Physics of Solids, Nöthnitzer Strasse 40, 01187 Dresden, Germany.

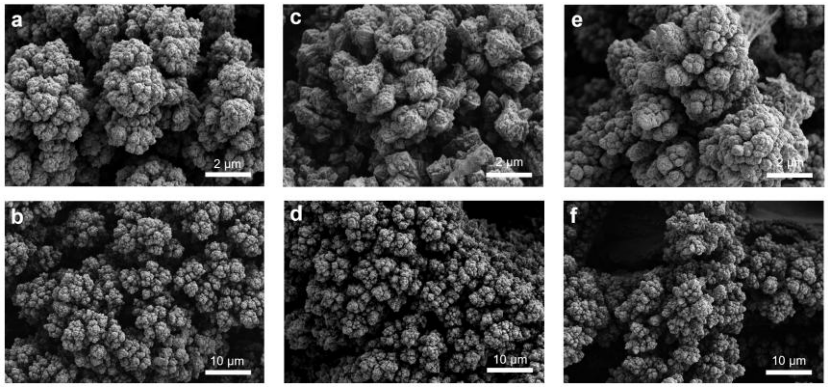

Supplementary Figure 1. SEM images of (a, b) Co_6Ni_4, (c, d) Co, and (e, f) Ni catalysts.

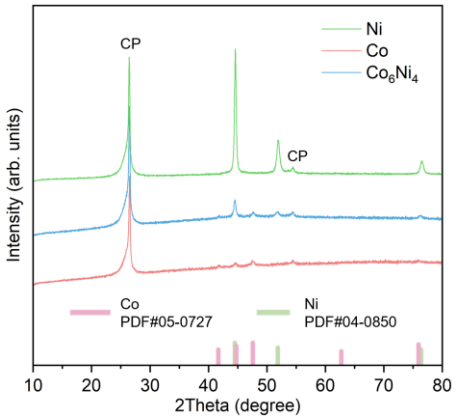

Supplementary Figure 2. XRD patterns of Co_6Ni_4, Co, and Ni catalysts. Source data for the above figure are provided as a Source Data file.

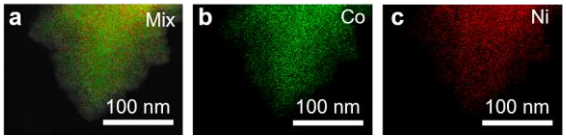

Supplementary Figure 3. (a-c) TEM-EDS elemental mappings of Co_6Ni_4.

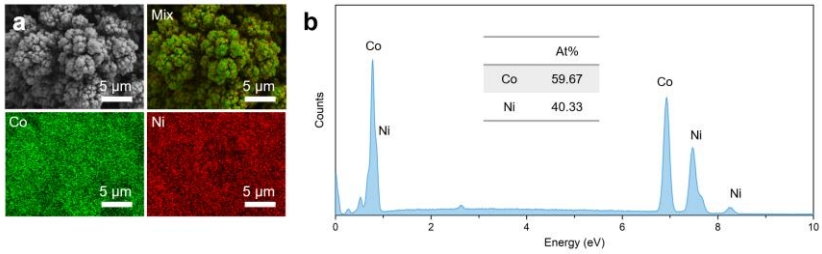

Supplementary Figure 4. (a) SEM-EDS elemental mappings and (b) element spectrum of Co_6Ni_4. Source data for the figure (b) are provided as a Source Data file.

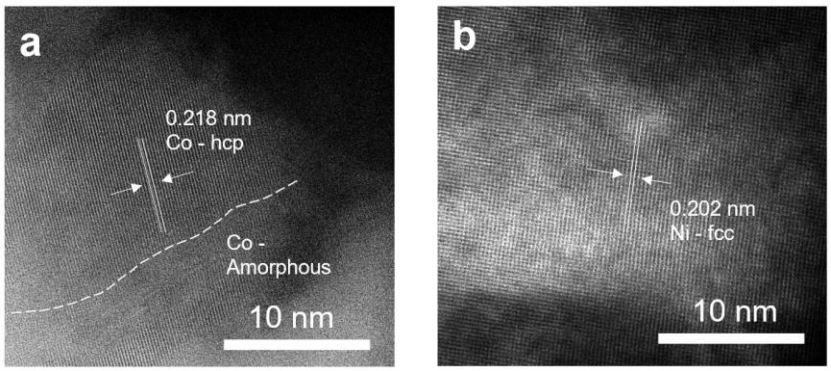

Supplementary Figure 5. (a, b) AC-HAADF-STEM images of Co_6Ni_4.

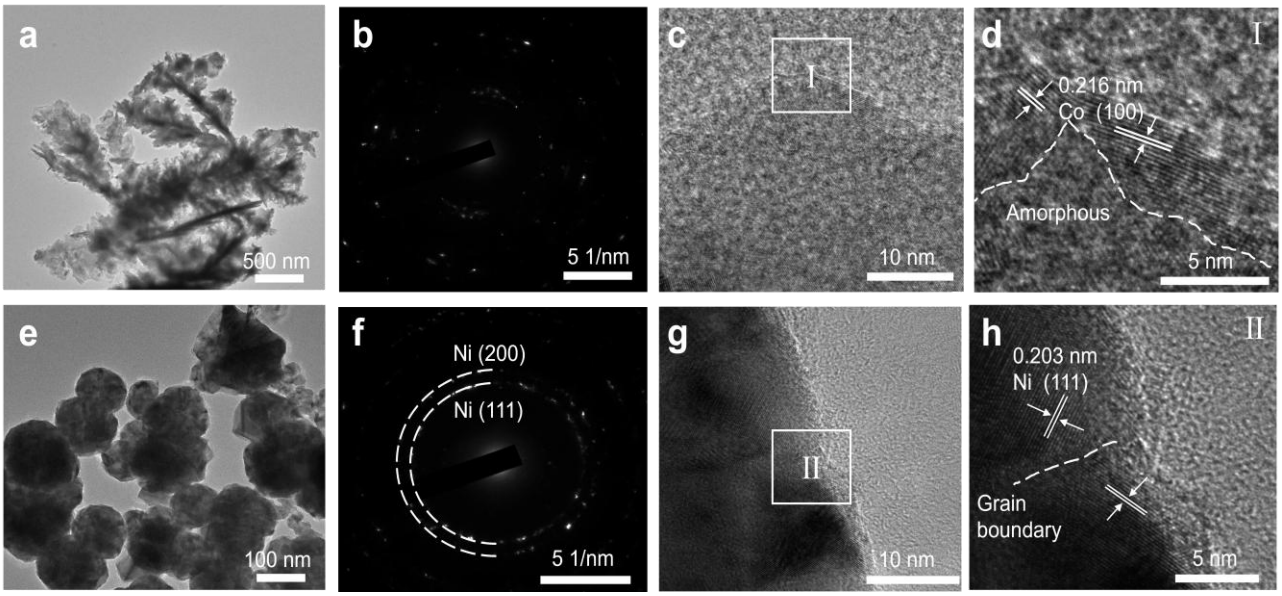

Supplementary Figure 6. (a) TEM image, (b) SAED pattern, and (c-d) HRTEM images for Co catalyst. (e) TEM image, (f) SAED pattern, and (g-h) HRTEM images for Ni catalyst. Figure d and h corresponds to area I in Figure c and area II in Figure g, respectively.

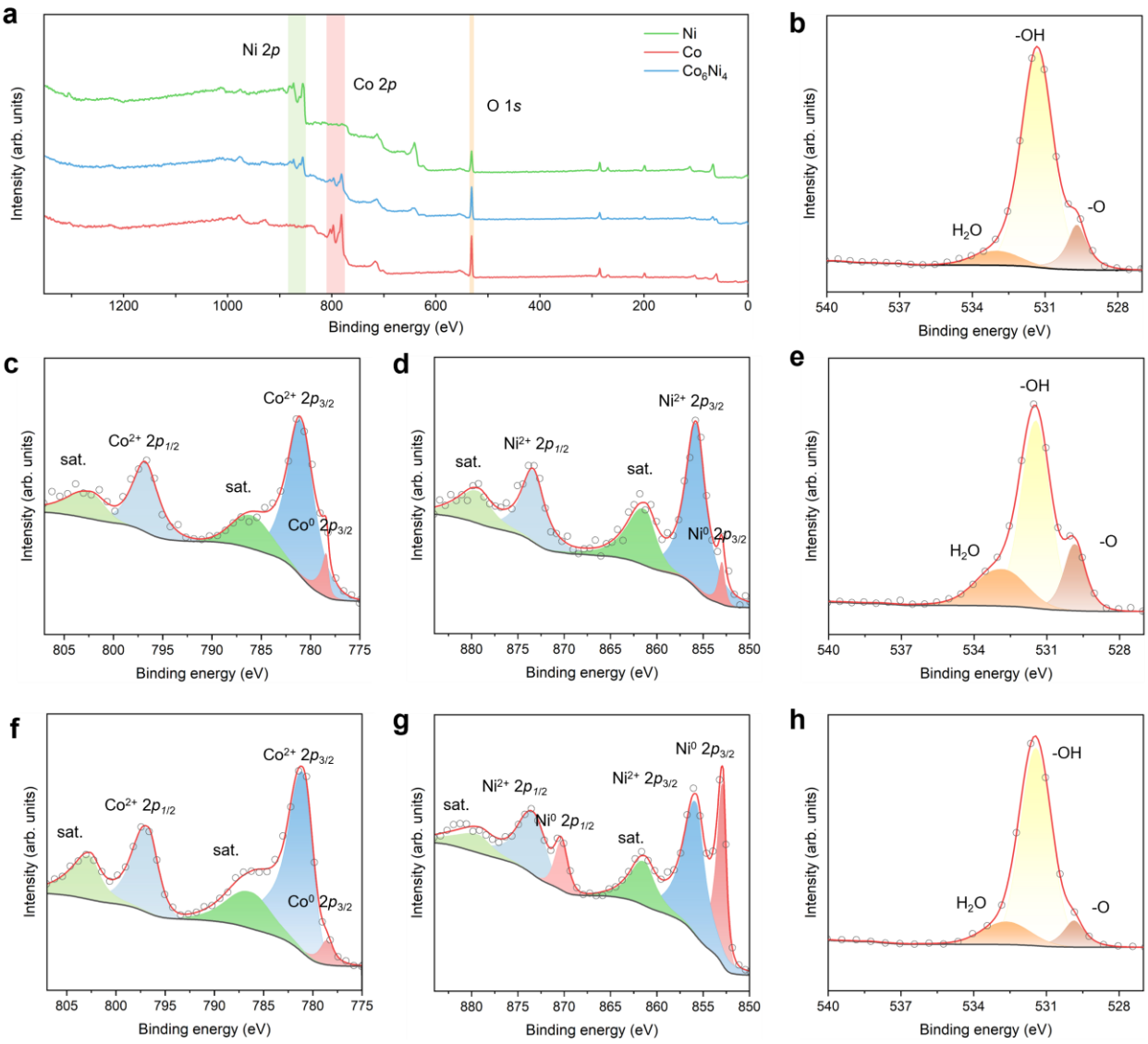

Supplementary Figure 7. (a) XPS survey spectra of Co_6Ni_4, Co, and Ni catalysts. (b) O 1s, (c) Co 2p, and (d) Ni 2p XPS spectra of Co_6Ni_4 catalysts. (e) O 1s and (f) Co 2p XPS spectra of Co catalyst. (g) Ni 2p and (h) O 1s XPS spectra of Ni catalyst. Source data for the above figures are provided as a Source Data file.

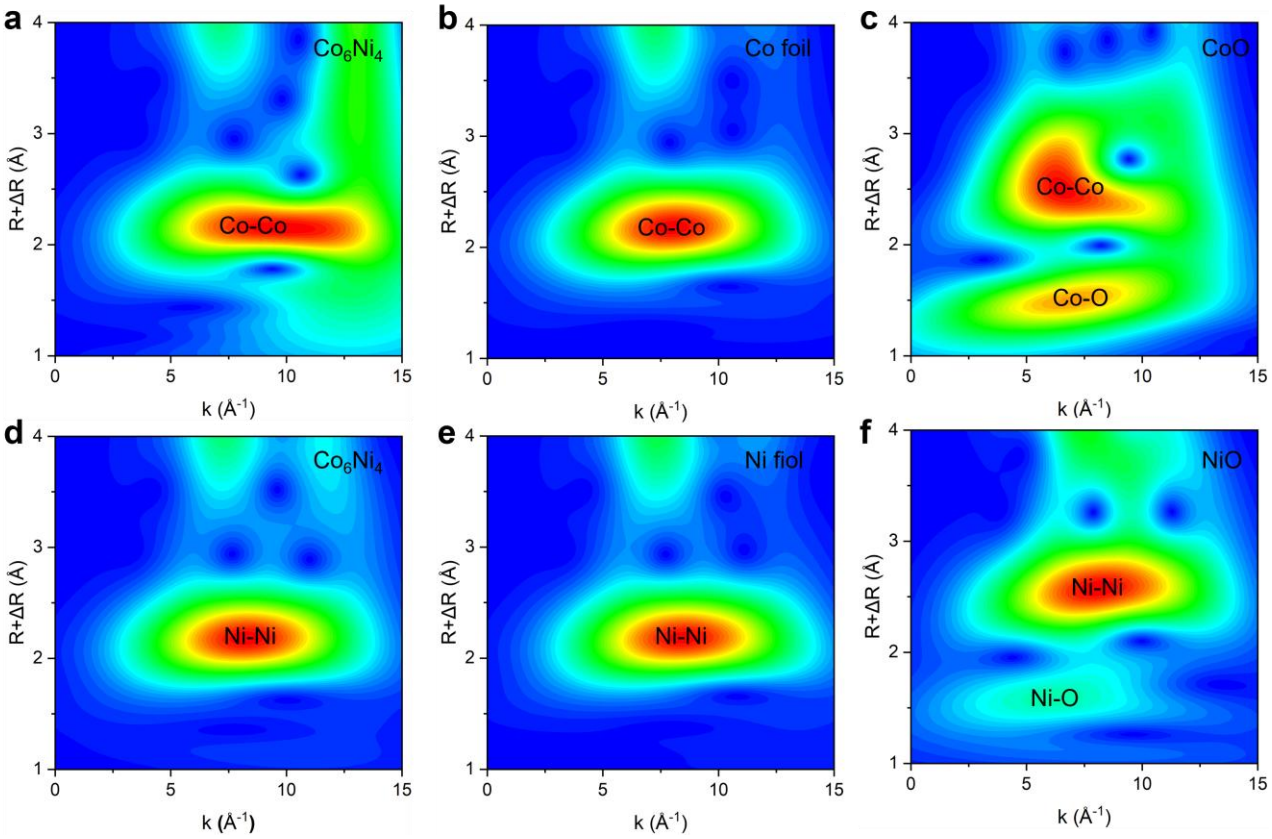

Supplementary Figure 8. Wavelet transforms of the k^3-weighted EXAFS signals for the Co element in (a) Co_6Ni_4 catalyst, (b) Co foil, and (c) CoO reference. Wavelet transforms of the k^3-weighted EXAFS signals for the Ni element in (d) Co_6Ni_4 catalyst, (e) Ni foil, and (f) NiO reference. Source data for the above figures are provided as a Source Data file.

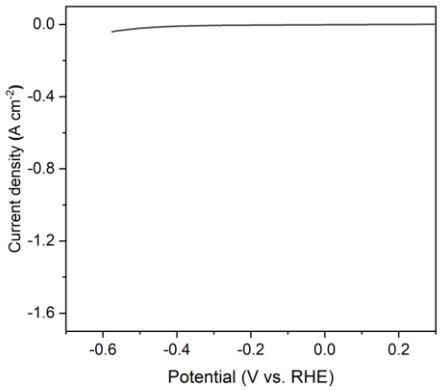

Supplementary Figure 9. LSV curve of CP for NO_3RR (without iR compensation). Source data for the above figure are provided as a Source Data file.

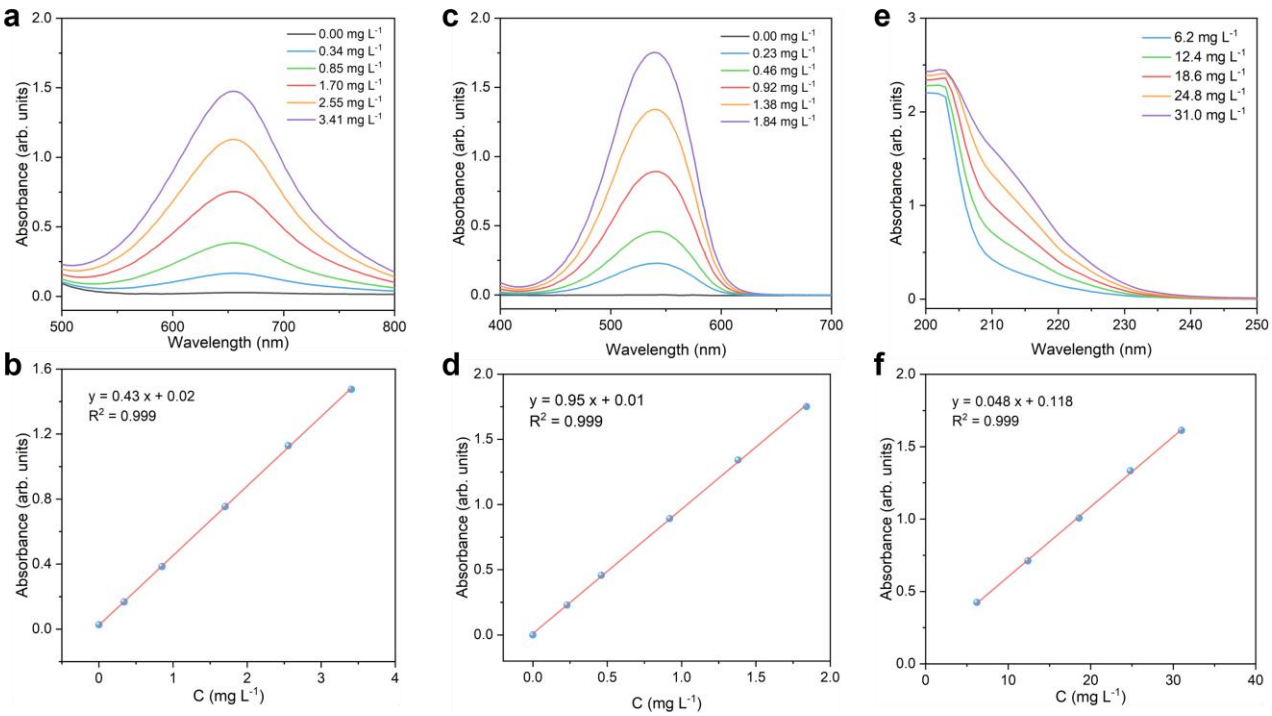

Supplementary Figure 10. UV-vis absorption spectra of the standard solution containing different concentrations of (a) NH_3, (c) NO_2^-, and (e) NO_3^-. The standard calibration curves for (b) NH_3, (d) NO_2^-, and (f) NO_3^-. Source data for the above figures are provided as a Source Data file.

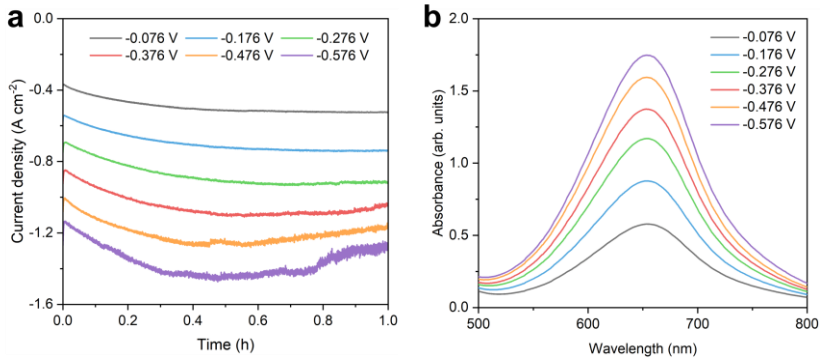

Supplementary Figure 11. (a) Chronoamperograms of Co_6Ni_4 catalyst for NO_3RR at different potentials (without iR compensation). (b) UV-vis spectra for quantifying the FE of NH_3 at various potentials on Co_6Ni_4 catalyst (potentials are not iR-corrected). Source data for the above figures are provided as a Source Data file.

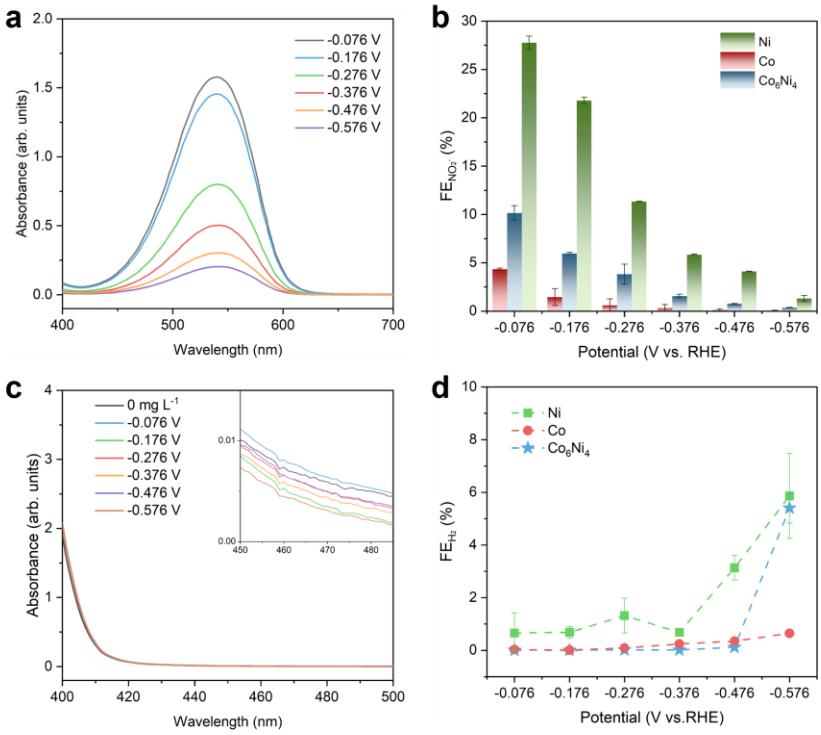

Supplementary Figure 12. UV-vis spectra for quantifying the FE of (a) NO_2^- and (c) N_2H_4 at various potentials on Co_6Ni_4 catalyst (potentials are not iR-corrected). The FE of (b) NO_2^- and (d) H_2 for NO_3RR on synthesized catalysts at various applied potentials (without iR compensation). The error bar represents the standard deviation of the data from three independent measurements. Source data for the above figures are provided as a Source Data file.

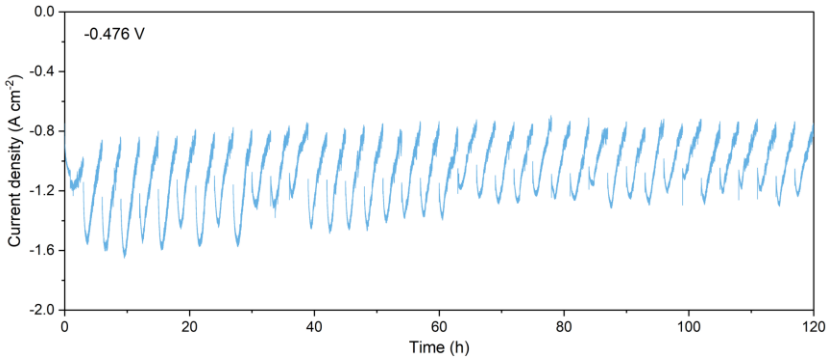

Supplementary Figure 13. Chronoamperometric measurement of Co_6Ni_4 for NO_3RR at -0.476 V (vs. RHE) (without iR compensation) over 40 consecutive cycles. Source data for the above figure are provided as a Source Data file.

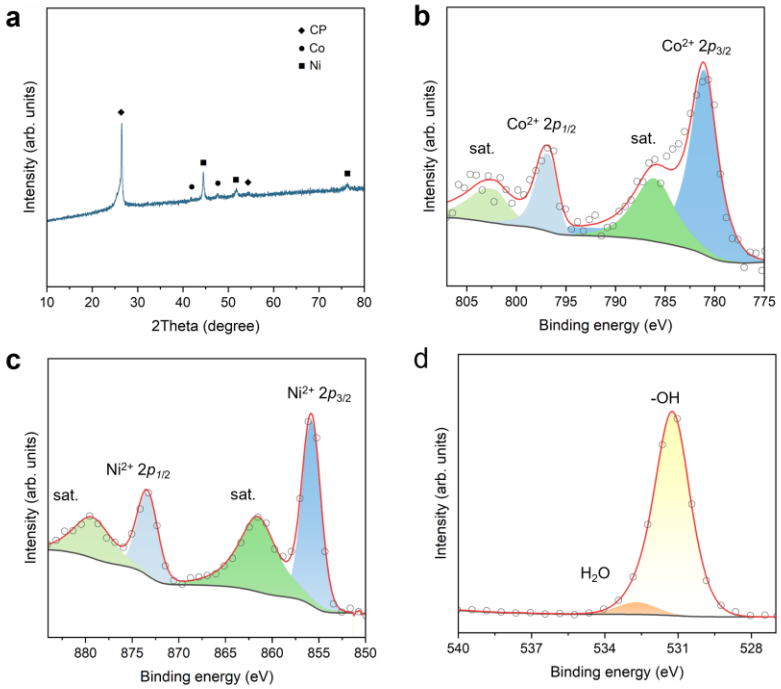

Supplementary Figure 14. (a) XRD pattern, (b) Co 2p XPS spectrum, (c) Ni 2p XPS spectrum, and (d) O 1s XPS spectrum of Co_6Ni_4 catalyst after 120-h NO_3RR. Source data for the above figures are provided as a Source Data file.

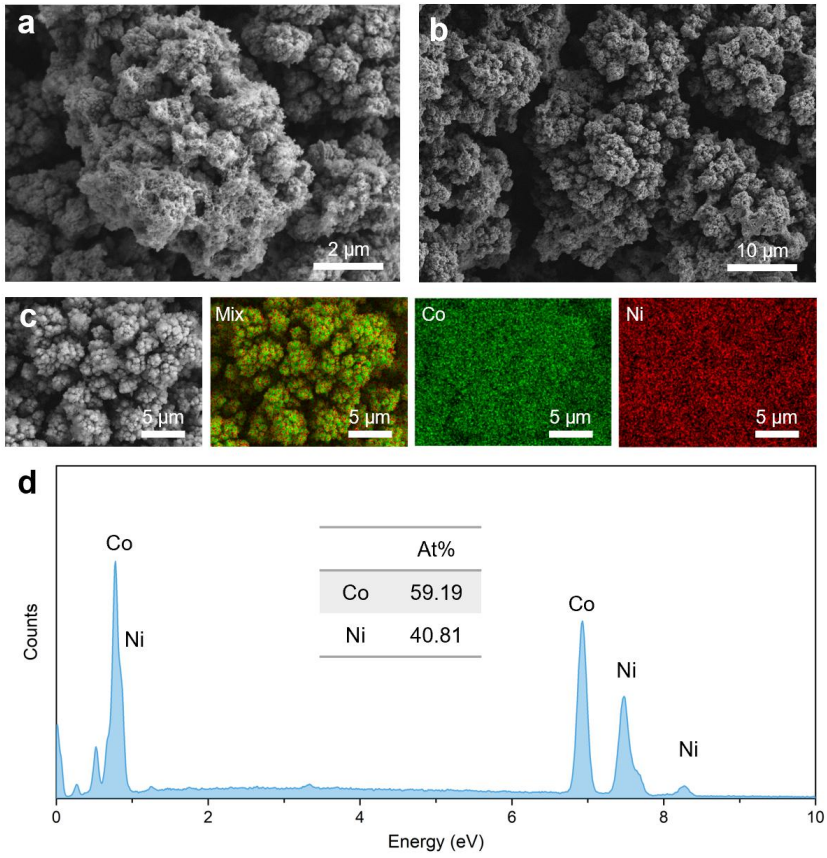

Supplementary Figure 15. (a-b) SEM images, (c) EDS elemental mappings, and (d) elemental analysis of Co_6Ni_4 catalyst after 120-h NO_3RR. Source data for the figure (d) are provided as a Source Data file.

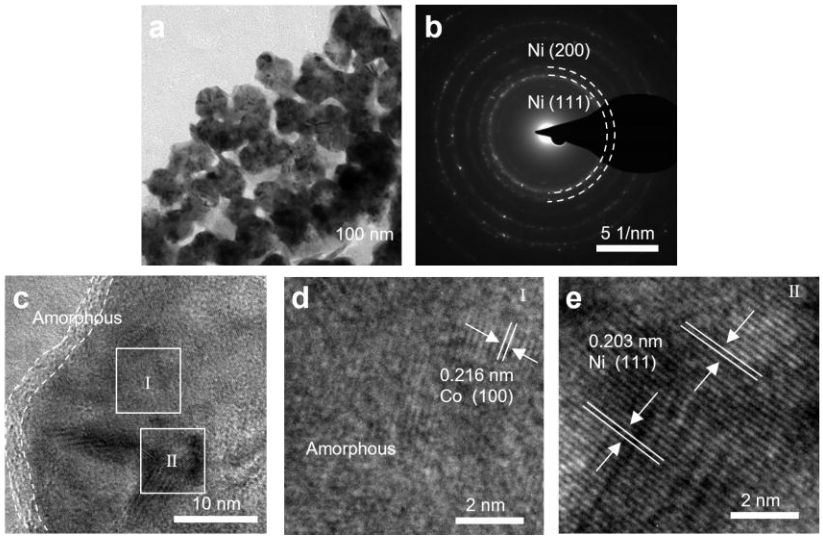

Supplementary Figure 16. (a) TEM image, (b) SAED pattern, and (c-e) HR-TEM images of Co_6Ni_4 after 120-h NO_3RR. Figures d and e correspond to areas I and II in Figure c, respectively.

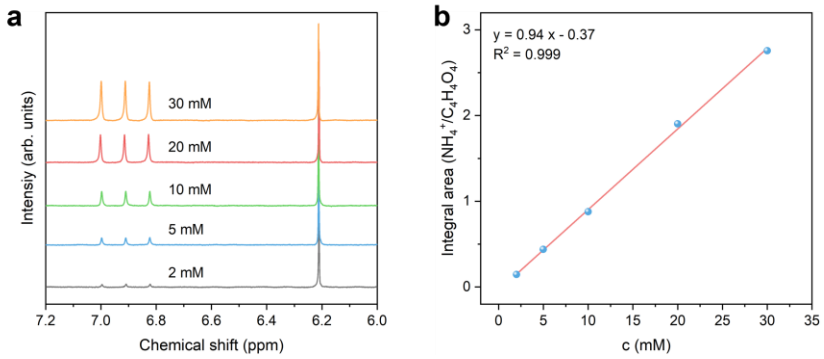

Supplementary Figure 17. (a) ^{1}H NMR calibration results for the quantification of NH_4^+. (b) The integral area is normalized by $C_4H_4O_4$. Source data for the above figures are provided as a Source Data file.

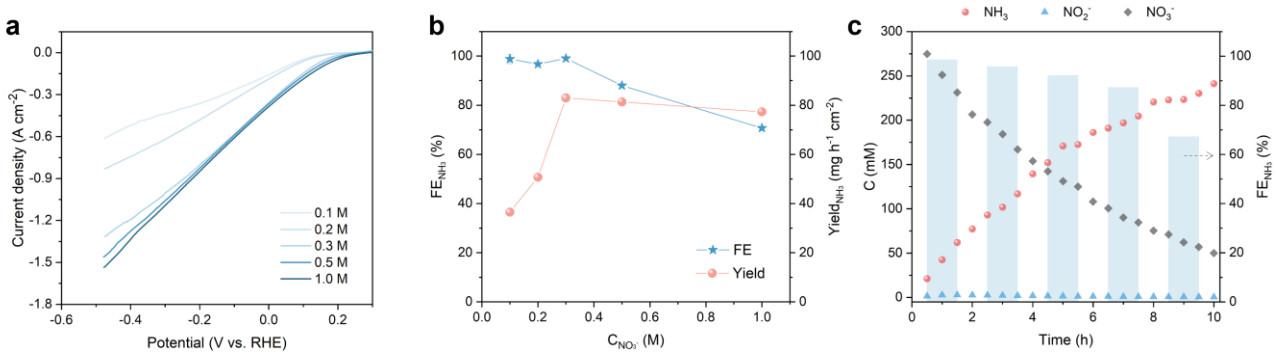

Supplementary Figure 18. (a) LSV curves of NO_3RR in different KNO_3 concentrations using Co_6Ni_4 as the catalyst (without iR compensation). (b) FE and yield of NH_3 for Co_6Ni_4 catalyst in different KNO_3 concentrations at -0.376 V (vs. RHE) (without iR compensation). The error bar represents the standard deviation of the data from three independent measurements. (c) Time-dependent FE_{NH3} variations and concentration changes of NO_3^-, NO_2^-, and NH_3 at -0.376 V (vs. RHE) (without iR compensation) for Co_6Ni_4. Source data for the above figures are provided as a Source Data file.

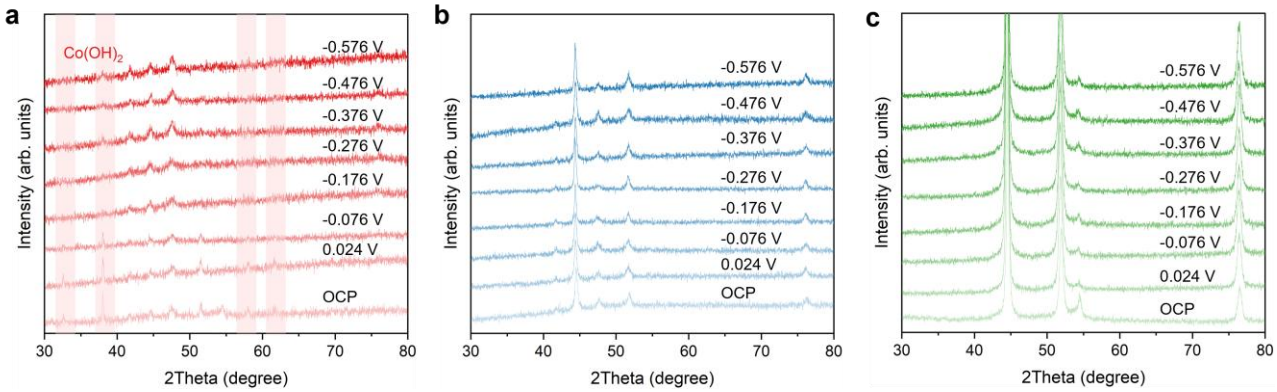

Supplementary Figure 19. Ex-situ XRD patterns of (a) Co, (b) Co_6Ni_4, and (c) Ni catalysts under NO_3RR conditions (potentials are not iR-corrected). XRD results were obtained by measuring the above catalysts at various potentials after 1h NO_3RR. Source data for the above figures are provided as a Source Data file.

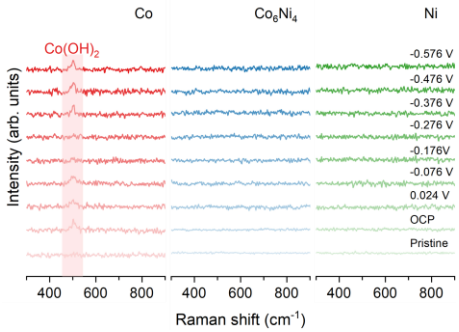

Supplementary Figure 20. In-situ Raman spectra for NO_3RR of Co_6Ni_4, Co, and Ni electrocatalysts (potentials are not iR-corrected). Source data for the above figure are provided as a Source Data file.

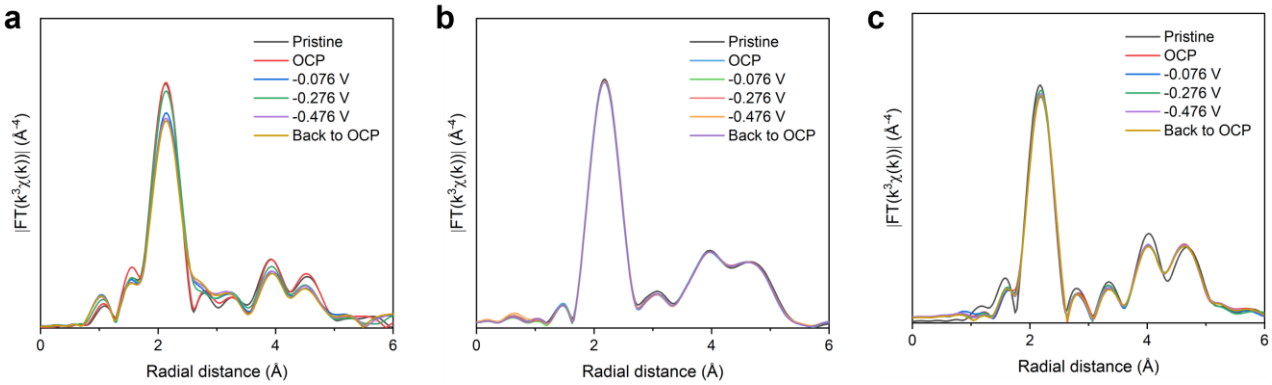

Supplementary Figure 21. R-space of (a) Co and (b) Co_6Ni_4 catalysts from operando EXAFS tests at the Co *K*-edge (potentials are not iR-corrected). (c) R-space of Co_6Ni_4 catalyst from operando EXAFS measurement at the Ni *K*-edge (potentials are not iR-corrected). Source data for the above figures are provided as a Source Data file.

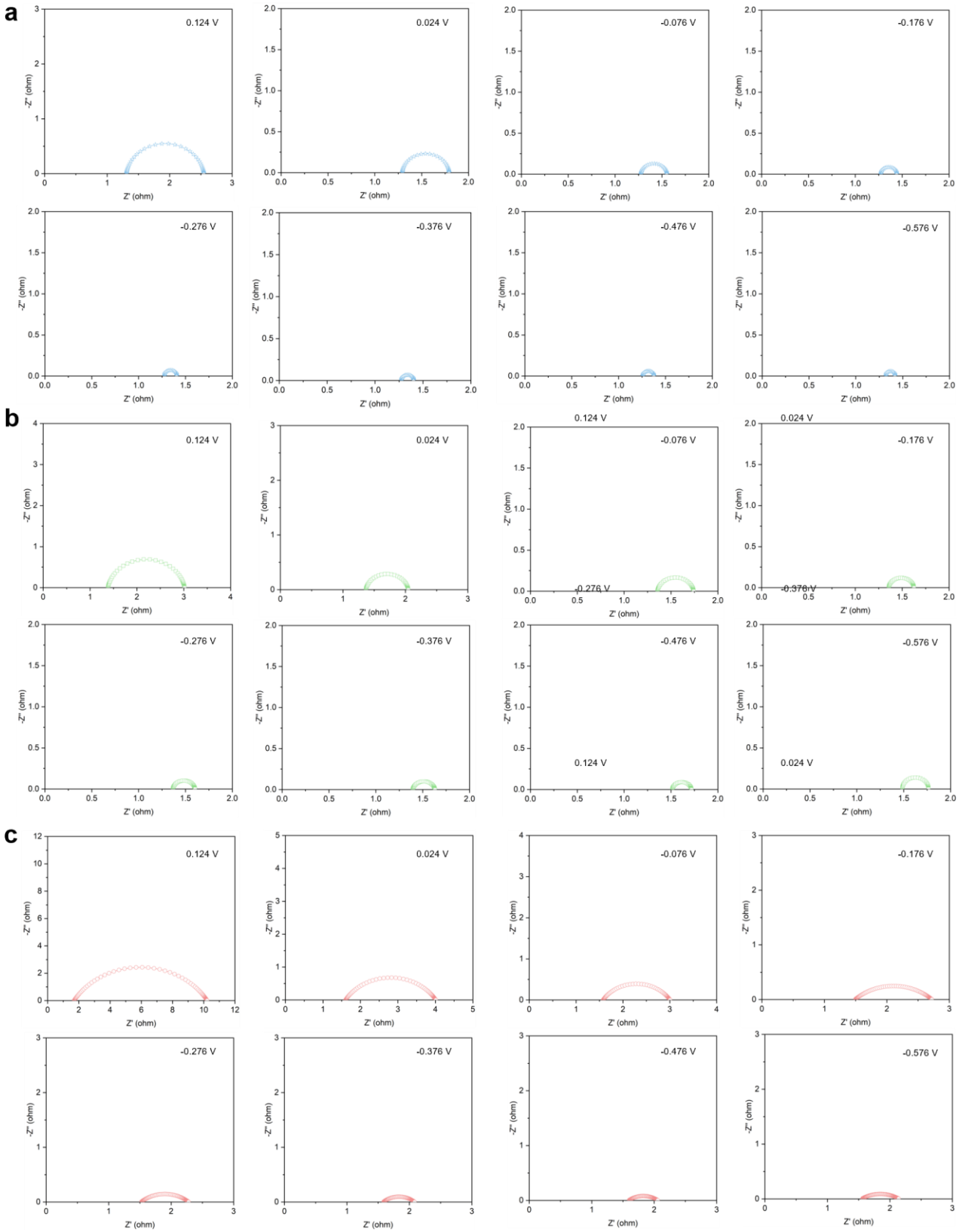

Supplementary Figure 22. Nyquist plots at various potentials (without iR compensation) calculated from in-situ EIS measurement for NO_3RR on (a) Co_6Ni_4, (b) Ni, and (c) Co catalysts. Source data for the above figures are provided as a Source Data file.

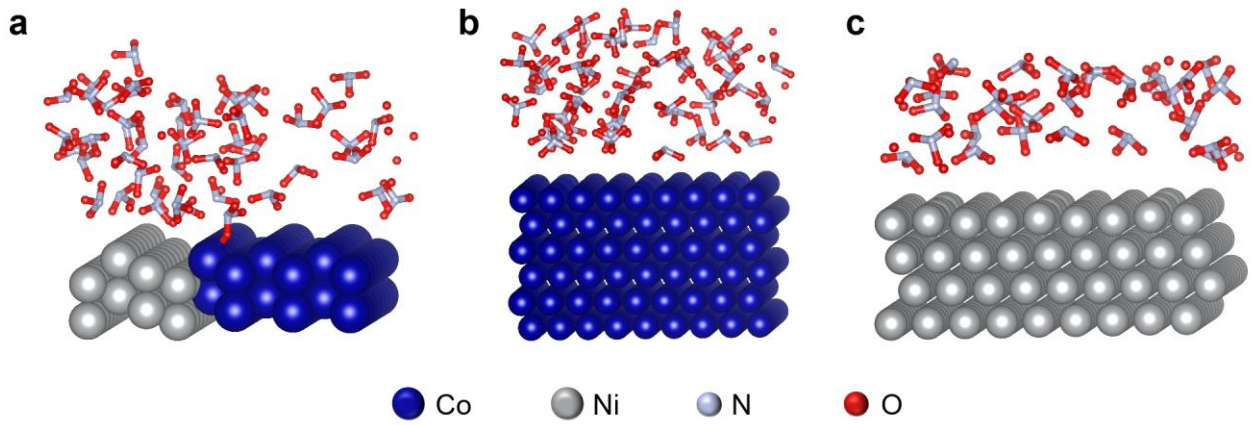

Supplementary Figure 23. The model of NO_3^- adsorption conditions at different potentials on (a) Co_6Ni_4, (b) Co, and (c) Ni.

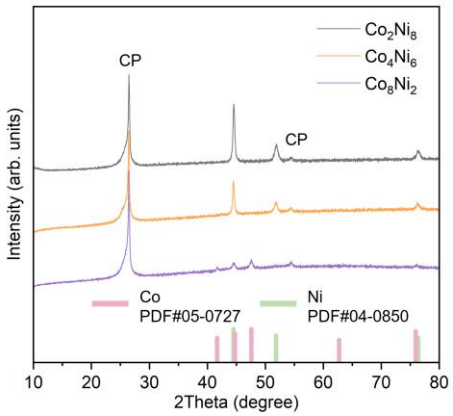

Supplementary Figure 24. XRD patterns of Co_8Ni_2, Co_4Ni_6, and Co_2Ni_8 catalysts. Source data for the above figure are provided as a Source Data file.

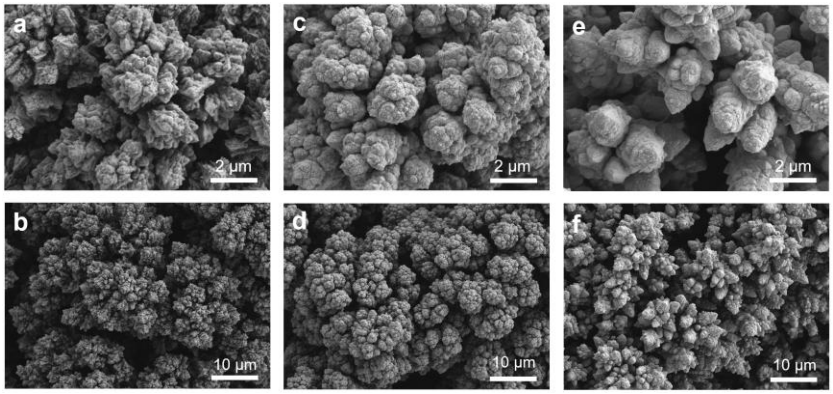

Supplementary Figure 25. SEM images of (a-b) Co_8Ni_2, (c-d) Co_4Ni_6, and (e-f) Co_2Ni_8 catalysts.

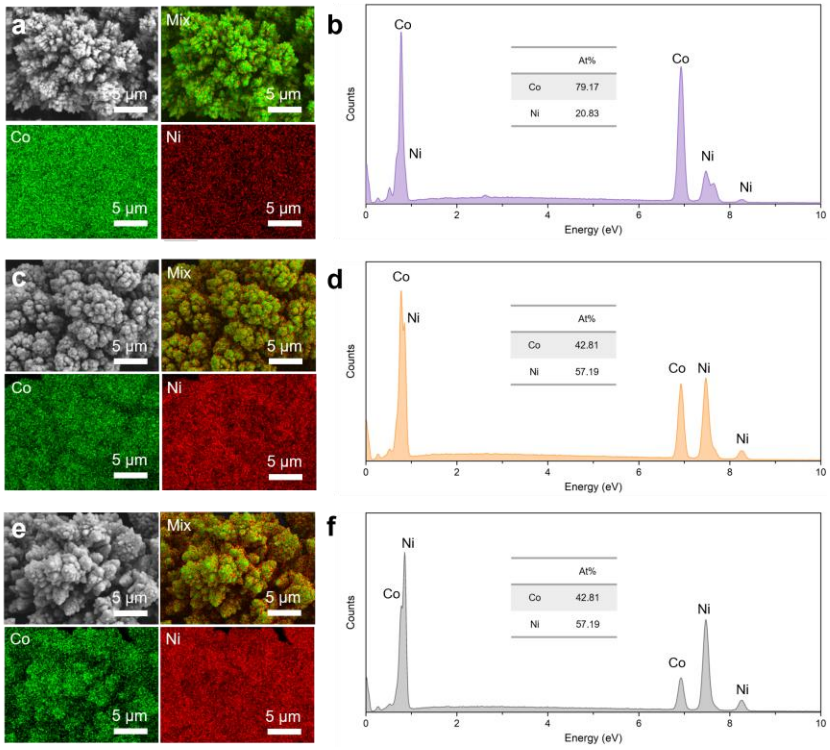

Supplementary Figure 26. EDS elemental mappings of (a) Co_8Ni_2, (c) Co_4Ni_6, and (e) Co_2Ni_8 catalysts. The content of Co and Ni determined by EDS for (b) Co_8Ni_2, (d) Co_4Ni_6, and (f) Co_2Ni_8 catalysts. Source data for the figures (b,d,f) are provided as a Source Data file.

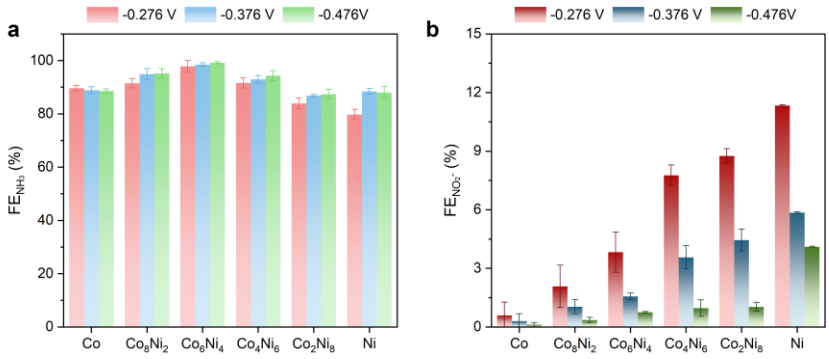

Supplementary Figure 27. The FE of (a) NH_3 and (b) NO_2^- for prepared catalysts against applied potentials (without iR compensation). The error bar represents the standard deviation of the data from three independent measurements. Source data for the above figures are provided as a Source Data file.

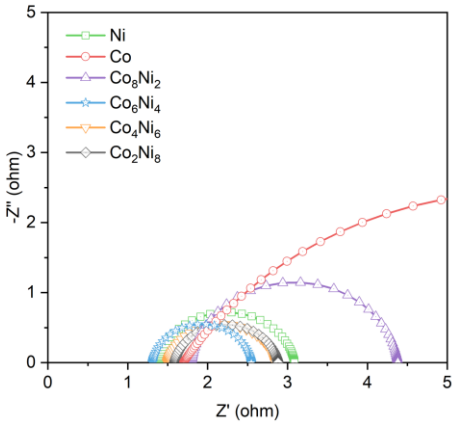

Supplementary Figure 28. The EIS Nyquist plots of NO_3RR of synthesized catalysts. Source data for the above figure are provided as a Source Data file.

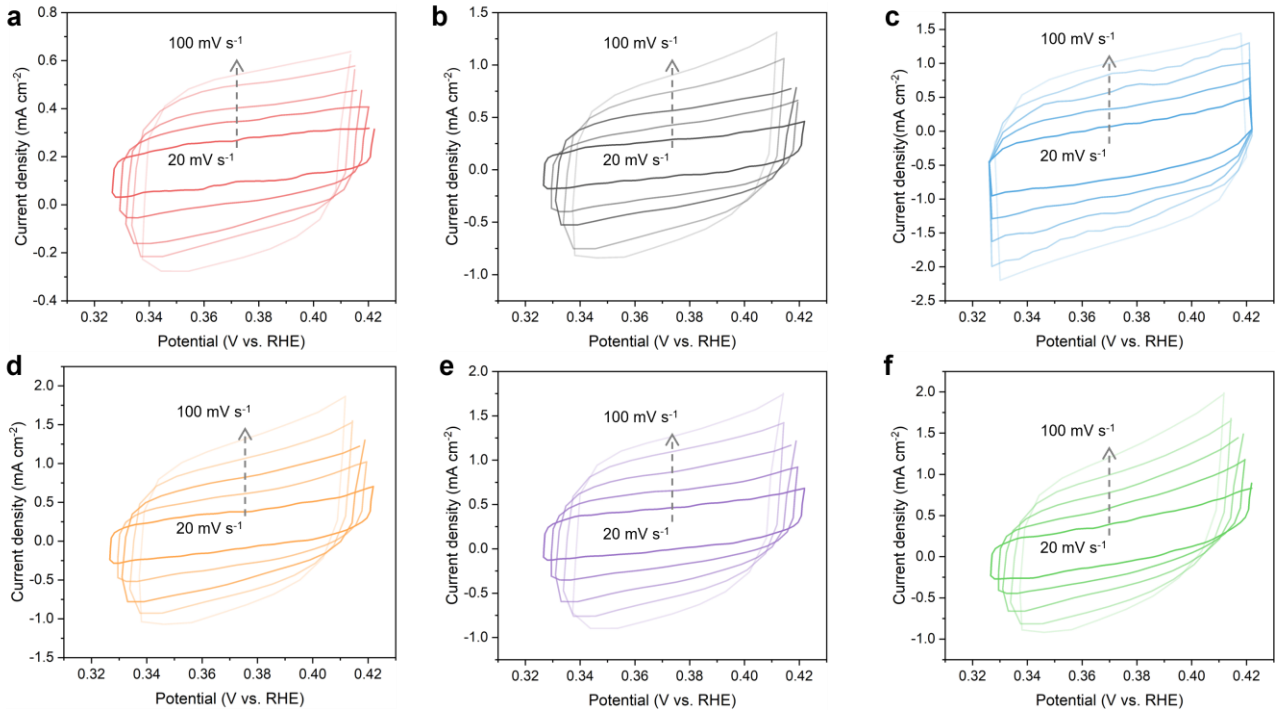

Supplementary Figure 29. CV curves (without iR compensation) of (a) Co, (b) Co_8Ni_2, (c) Co_6Ni_4, (d) Co_4Ni_6, (e) Co_2Ni_8, and (f) Ni catalysts are collected at various scan rates in 1 M KOH + 0.3 M KNO_3. Source data for the above figures are provided as a Source Data file.

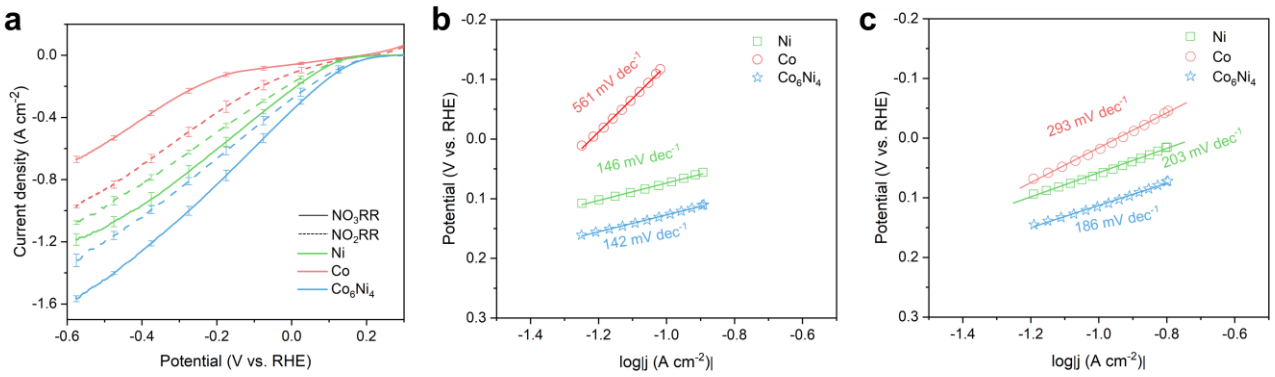

Supplementary Figure 30. (a) LSV curves of Co_6Ni_4, Co, and Ni catalysts for NO_3RR and NO_2RR (without iR compensation). Tafel slopes of Co_6Ni_4, Co, and Ni catalysts for (b) NO_3RR and (c) NO_2RR. The error bar represents the standard deviation of the data from three independent measurements (potentials are not iR-corrected). Source data for the above figures are provided as a Source Data file.

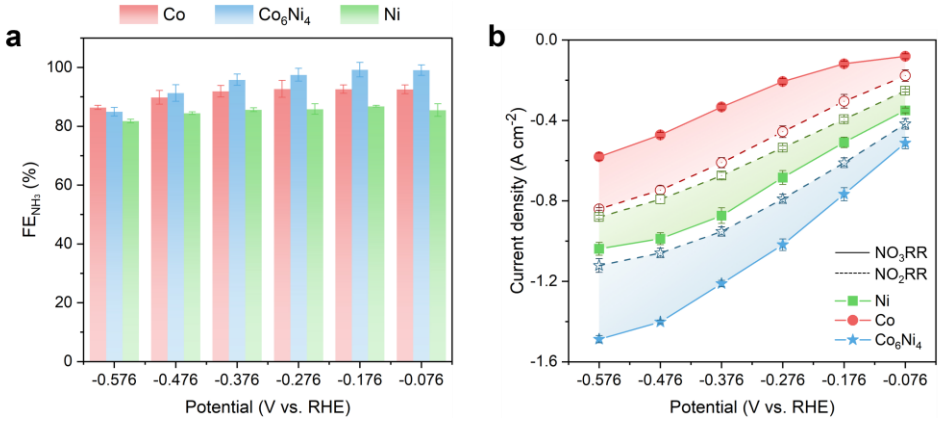

Supplementary Figure 31. (a) The FE_{NH_3} of Co_6Ni_4, Co, and Ni catalysts for NO_2RR (potentials are not iR-corrected). (b) The current density of main product for NO_2RR and NO_3RR on Co_6Ni_4, Co, and Ni catalysts (potentials are not iR-corrected). The primary product of NO_2RR is NH_3, and the primary products of NO_3RR are NH_3 and NO_2^-. The error bar represents the standard deviation of the data from three independent measurements. Source data for the above figures are provided as a Source Data file.

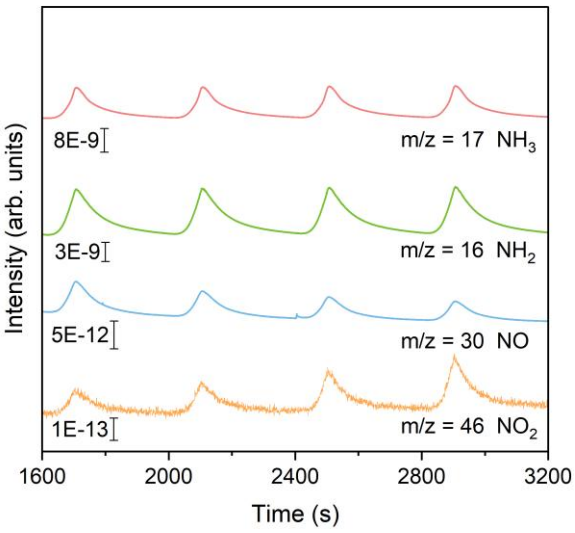

Supplementary Figure 32. Online DEMS of Co_6Ni_4 during NO_3RR. Source data for the above figure are provided as a Source Data file.

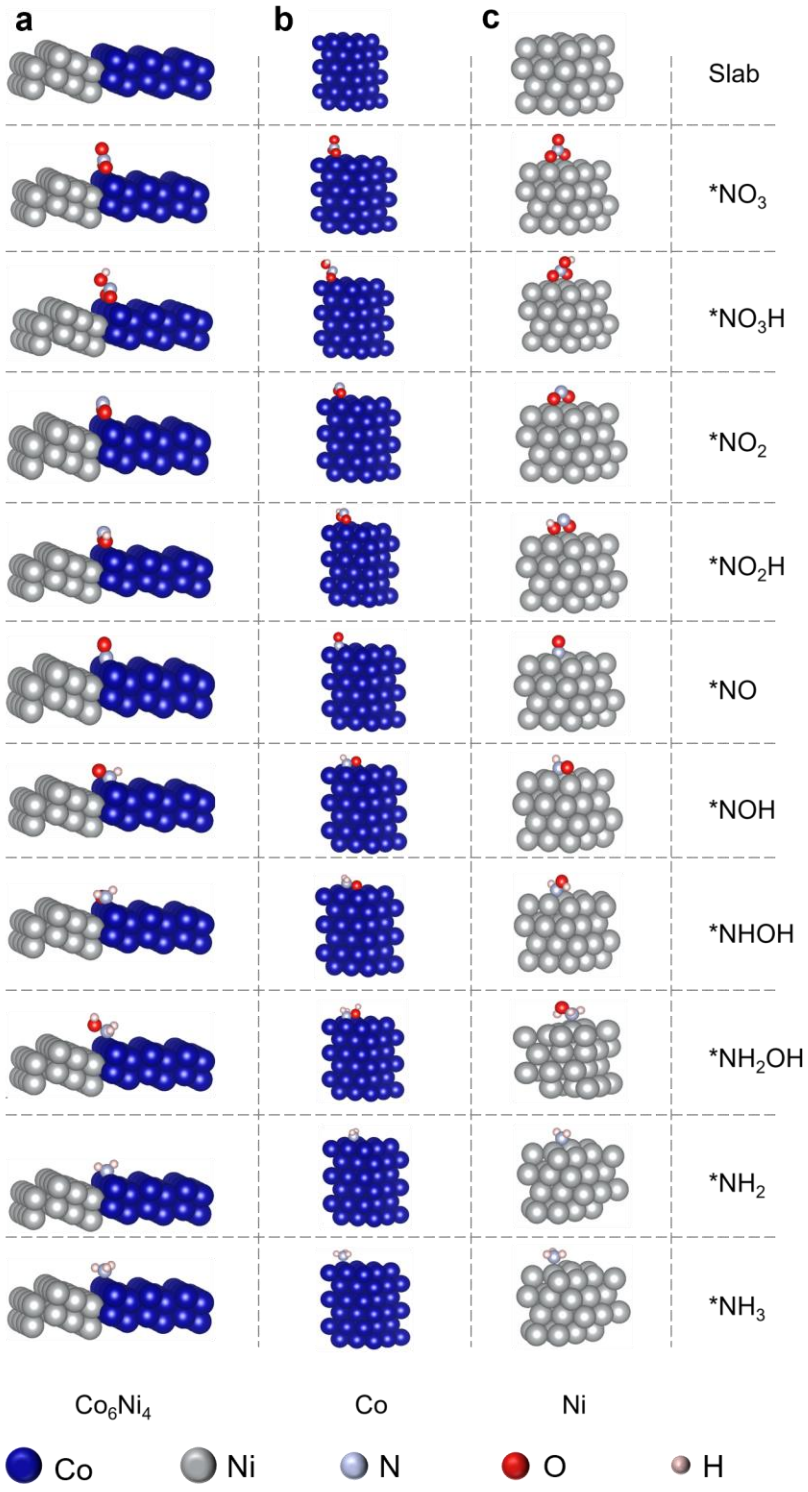

Supplementary Figure 33. The Gibbs free energy calculation models of adsorbed intermediates for NO_3RR on (a) Co_6Ni_4, (b) Co, and (c) Ni.

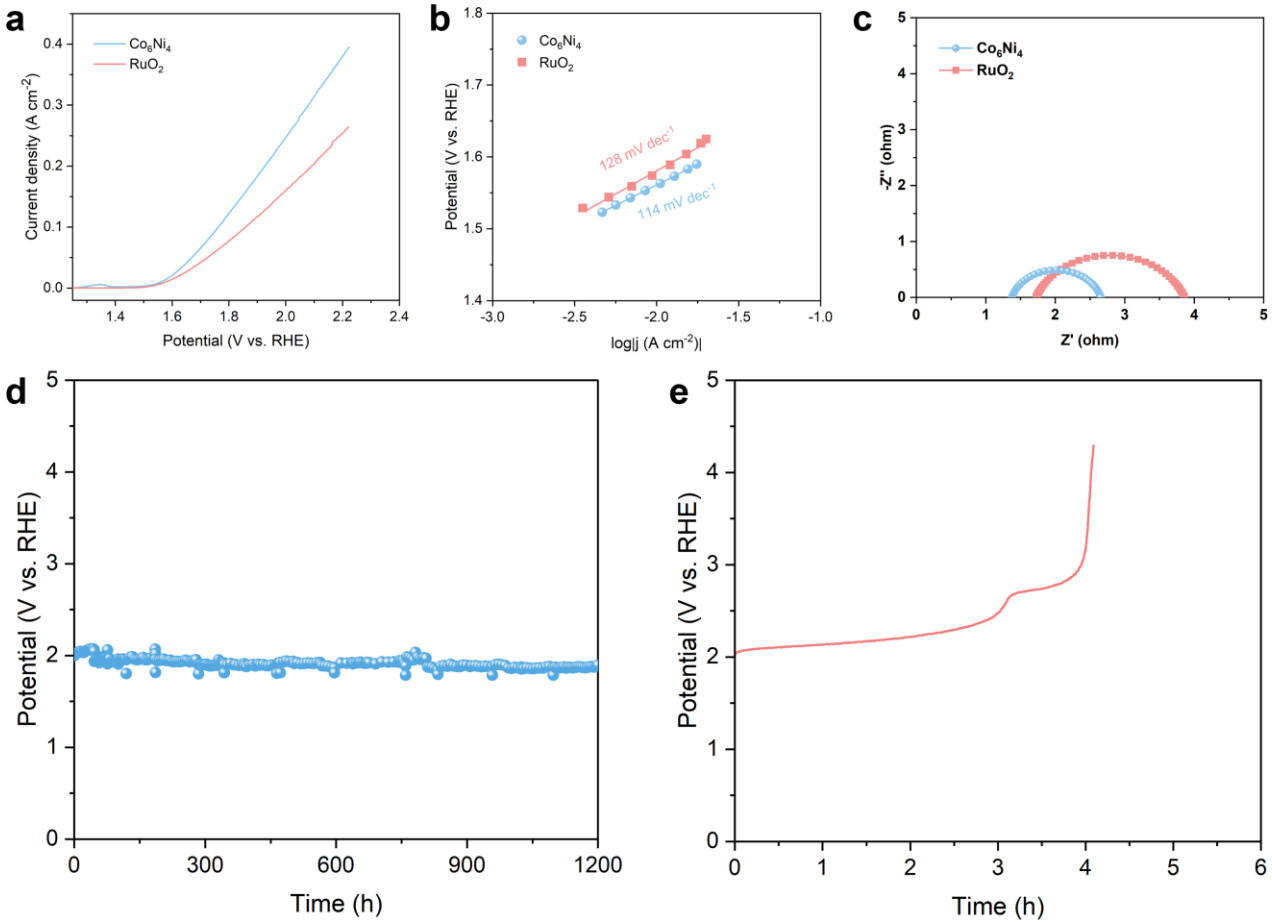

Supplementary Figure 34. The (a) LSV curves (without iR compensation), (b) Tafel slopes (potentials are not iR-corrected), and (c) Nyquist plot of OER in 1 M KOH for Co_6Ni_4 and RuO_2. The OER stability test at 250 mA cm^{-2} for (d) Co_6Ni_4 and (e) RuO_2 (potentials are not iR-corrected). Source data for the above figures are provided as a Source Data file.

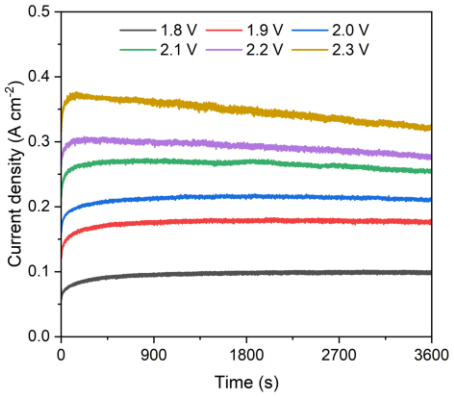

Supplementary Figure 35. I-t curves of Co_6Ni_4 for MEA at different cell voltages (without iR compensation). Source data for the above figure are provided as a Source Data file.

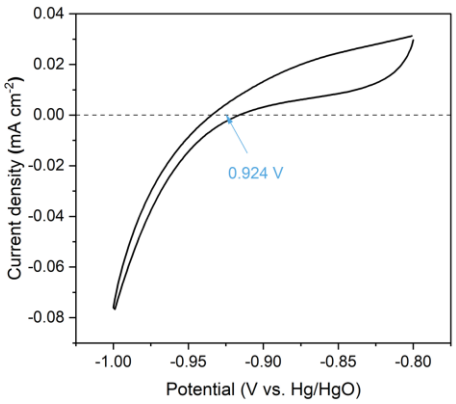

Supplementary Figure 36. Potential (without iR compensation) calibration of the Hg/HgO reference electrode in H_2-saturated 1 M KOH solution at 25 °C. Source data for the above figure are provided as a Source Data file.

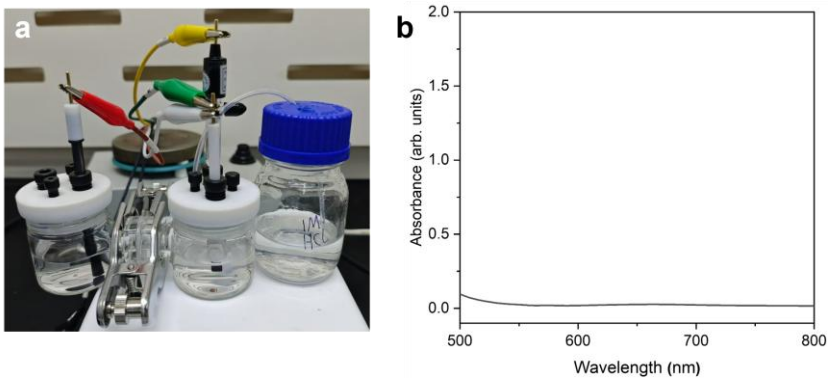

Figure 37. (a) Schematic of the reactor for the NH_3 overflow detection. (b) UV-vis spectrum for the HCl solution after capturing the escaped NH_3. Source data for the above figure are provided as a Source Data file.

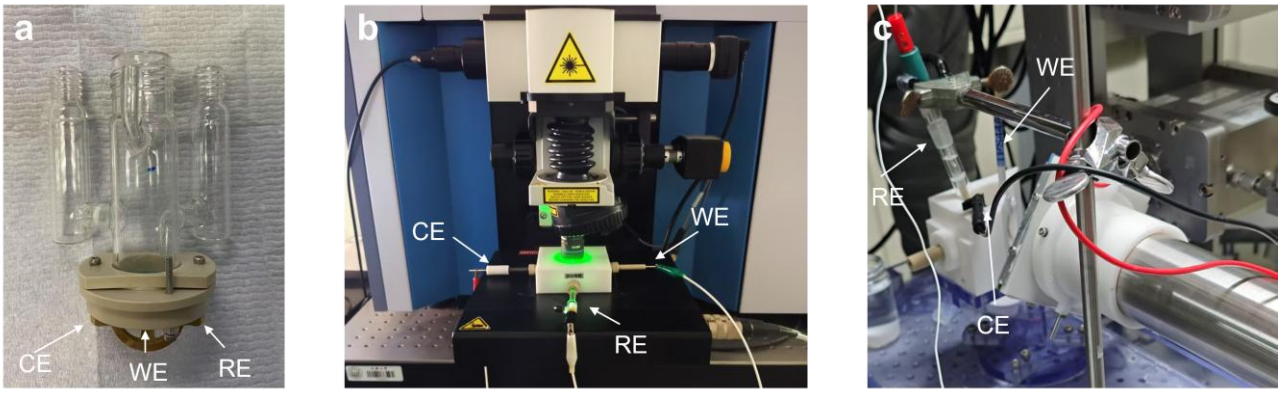

Figure 38. Schematic diagrams of the electrolytic cell setup for (a) in-situ FTIR, (b) in-situ Raman spectroscopy, and (c) operando XAS measurements.

Supplementary Table 1. ICP-OES results of Co_xNi_y catalysts.

	Co (at.%)	Ni (at.%)
Co	99.94	0.06
Co_8Ni_2	80.35	19.65
Co_6Ni_4	60.44	39.56
Co_4Ni_6	41.28	58.72
Co_2Ni_8	19.99	80.01
Ni	0.13	99.87

Supplementary Table 2. Comparison of the NO_3RR performance of recently reported electrocatalysts.

Catalyst	Potential @ 1A cm^{-2} (V vs. RHE)	E (V vs. RHE)	FE_{NH3} (%)	$Yield_{NH3}$ ($mg\ h^{-1}\ cm^{-2}$)	Stability (h)	Electrolyte	Ref.
Co_6Ni_4	-0.276	-0.476	99.21	93.55	120	0.3 M KNO_3 + 1 M KOH	This work
NiCoP	-0.48 100% iR	-0.3 100% iR	99.7	55.33	24	1.0 M KNO_3 + 1 M KOH	1
RuPt/Cu	--	-0.2	99.8	58.76	62	1.0 M KNO_3 + 1 M KOH	2
Co_3O_4/Cu-N-C	-0.71 50% iR	-0.8 50% iR	97.7	92.46	20	1.0 KNO_3 + 1 M KOH	3
SP-Fe1-Ti	--	-0.4	95.2	68.12	40	1.0 M $NaNO_3$ + 1 M KOH	4
CoP-CNS	--	-1.03	90	52.63	123	1.0 M KNO_3 + 1 M KOH	5
Cu_1Co_5	--	0.075 80% iR	96.2	32.4	30	1.0 M KNO_3 + 1 M KOH	6
CoP NAs/CFC	--	-0.3	99.3	16.89	60	1.0 M $NaNO_3$ + 1 M NaOH	7
CuPc MDE	-0.6 85% iR	-0.32 85% iR	98.4	62.4	30	1.0 M $NaNO_3$ + 1 M NaOH	8
CuPd	--	-0.5	92.5	21.29	12	1.0 M KNO_3 + 1 M KOH	9
CuNi NPs/CF	-0.38	-0.48	97.03	94.57	12	0.71 M $NaNO_3$ + 1 M NaOH	10
Cu_1Co_1	-0.5	-0.5	96.15	78.77	20	0.5 M KNO_3 + 1 M KOH	11
Au skin-Au Cu_3	--	0.55	96	12.94	110	0.5 M KNO_3 + 1 M KOH	12
CoP@Co	--	-0.2 100% iR	96.7	17.88	5	0.5 M KNO_3 + 1 M KOH	13
Pd-Cl/Cu_2O	-0.5	-0.6	97.5	53.46	10	0.5 M KNO_3 + 1 M KOH	14
Ni/$Ni(OH)_2$	-0.53	-0.467	98.5	84.74	102	0.5 M KNO_3 + 1 M KOH	15
Cu(100)/(111)	--	-0.36 85% iR	95	18.39	700	0.2 M KNO_3 + 1 M KOH	16
$CuCo_2O_4$	-0.84	-0.8	96.8	114.9	22	0.2 M NO_X^- + 1 M NaOH	17
Fe_2O_3/Fe-N-C	-0.86	-1.0	100.7	115.81	24	0.16 M KNO_3 +	18

						1 M KOH	
P-Cu/$Co(OH)_2$	--	-0.4	97.04	42.63	12	0.1 M KNO_3 + 1 M KOH	19
Cu/β-$Co(OH)_2$	-0.6	-0.5	97.7	66.42	30	0.1 M KNO_3 + 1 M KOH	20
$Ni(OH)_2$/Ni	--	-0.8	98.99	47.85	50	0.1 M KNO_3 + 1 M KOH	21
Cu_3N/GDY	--	-0.9	98.1	35.28	5	0.1 M KNO_3 + 1 M KOH	22
Cu_9S_5-SNWs	--	-0.3 90% iR	90.4	6.3	20	0.1 M KNO_3 + 1 M KOH	23
Cu-N_4B_2	--	-0.6 100% iR	98.2	68.63	30	0.1 M KNO_3 + 1 M KOH	24
Fe-Ni_2P@NF	-0.6	-0.8	96.1	90.8	132	0.1 M KNO_3 + 1 M KOH	25

Note: the FE_{NH_3} in the table represents the highest FE_{NH_3} observed for the catalyst, and the corresponding E and $yield_{NH_3}$ align with the highest FE.

Supplementary Table 3 The Gibbs free energies for NO_3RR intermediates on established modes of Co_6Ni_4, Co, and Ni catalysts.

	Co_6Ni_4 (eV)	Co (eV)	Ni (eV)
Slab	0	0	0
$*NO_3$	-3.5769	-0.8774	-1.5232
$*NO_3H$	-3.1933	-0.4873	-1.2483
$*NO_2$	-5.3585	-3.4601	-3.1139
$*NO_2H$	-5.0691	-3.1595	-2.8369
*NO	-7.1659	-5.5191	-5.5415
*NOH	-6.5400	-3.3323	-4.8550
*NHOH	-7.6490	-4.4443	-5.5014
$*NH_2OH$	-6.9664	-5.5665	-5.6590
$*NH_2$	-6.7048	-5.7993	-6.2900
$*NH_3$	-7.8818	-7.4818	-7.4818
NH_3	-7.2727	-7.3928	-7.3928

References

1. Li, Y. et al. Improved Nitrate-to-Ammonia Electrocatalysis through Hydrogen Poisoning Effects. *Angew. Chem. Int. Ed.* **63**, e202411068 (2024).
2. Li, Y. et al. Hydrogen Spillover Mechanism at the Metal–Metal Interface in Electrocatalytic Hydrogenation. *Angew. Chem. Int. Ed.* **63**, e202407810 (2024).
3. Liu, Y. et al. Efficient tandem electroreduction of nitrate into ammonia through coupling Cu single atoms with adjacent Co_3O_4. *Nat. Commun.* **15**, 3619 (2024).
4. Dai, J. et al. Spin polarized Fe_1−Ti pairs for highly efficient electroreduction nitrate to ammonia. *Nat. Commun.* **15**, 88 (2024).
5. Fan, K. et al. Active hydrogen boosts electrochemical nitrate reduction to ammonia. *Nat. Commun.* **13**, 7958 (2022).
6. Zhou, Y. et al. Boosting Electrocatalytic Nitrate Reduction to Ammonia via Promoting Water Dissociation. *ACS Catal.* **13**, 10846-10854 (2023).
7. Ye, S. et al. Elucidating the activity, mechanism and application of selective electrosynthesis of ammonia from nitrate on cobalt phosphide. *Energy Environ. Sci.* **15**, 760-770 (2022).
8. Jiang, Z. et al. Molecular electrocatalysts for rapid and selective reduction of nitrogenous waste to ammonia. *Energy Environ. Sci.* **16**, 2239-2246 (2023).
9. Gao, Q. et al. Breaking adsorption-energy scaling limitations of electrocatalytic nitrate reduction on intermetallic CuPd nanocubes by machine-learned insights. *Nat. Commun.* **13**, 2338 (2022).
10. Yu, W. et al. Laser-controlled tandem catalytic sites of CuNi alloys with ampere-level electrocatalytic nitrate-to-ammonia reduction activities for Zn–nitrate batteries. *Energy Environ. Sci.* **16**, 2991-3001 (2023).
11. Jang, W. et al. Homogeneously Mixed Cu–Co Bimetallic Catalyst Derived from Hydroxy Double Salt for Industrial-Level High-Rate Nitrate-to-Ammonia Electrosynthesis. *J. Am. Chem. Soc.* **146**, 27417-27428 (2024).
12. Xiao, Y. et al. Strained Au skin on Mesoporous Intermetallic $AuCu_3$ Nanocoral for Electrocatalytic Conversion of Nitrate to Ammonia across a Wide Concentration Range. *Angew. Chem. Int. Ed.* **63**, e202408758 (2024).
13. Yang, K. et al. Unveiling the Reaction Mechanism of Nitrate Reduction to Ammonia Over Cobalt-Based Electrocatalysts. *J. Am. Chem. Soc.* **146**, 12976-12983 (2024).
14. Liao, W. et al. Sustainable conversion of alkaline nitrate to ammonia at activities greater than 2 A cm^{-2}. *Nat. Commun.* **15**, 1264 (2024).
15. Shi, X. et al. Synergistic Effect of $Ni/Ni(OH)_2$ Core-Shell Catalyst Boosts Tandem Nitrate Reduction for Ampere-Level Ammonia Production. *Angew. Chem. Int. Ed.* **63**, e202406750 (2024).
16. Fu, Y. et al. Enhancing Electrochemical Nitrate Reduction to Ammonia over Cu Nanosheets via Facet Tandem Catalysis. *Angew. Chem. Int. Ed.* **62**, e202303327 (2023).
17. Gao, R. et al. A Bifunctional Catalyst for Green Ammonia Synthesis from Ubiquitous Air and Water. *Adv. Mater.* **35**, 2303455 (2023).
18. Murphy, E. et al. Synergizing Fe_2O_3 Nanoparticles on Single Atom Fe-N-C for Nitrate Reduction to Ammonia at Industrial Current Densities. *Adv. Mater.* **36**, 2401133 (2024).
19. Yan, Q. et al. Enhancing Compatibility of Two-Step Tandem Catalytic Nitrate Reduction to Ammonia Over P-Cu/$Co(OH)_2$. *Adv. Mater.* **36**, 2408680 (2024).
20. Qiao, L. et al. In Situ Reconstructed Cu/β-$Co(OH)_2$ Tandem Catalyst for Enhanced Nitrate

Electroreduction to Ammonia in Ampere-Level. *Adv. Energy Mater.* **14**, 2402805 (2024).
21. Lv, J. et al. Promoting the OH cycle on an activated dynamic interface for electrocatalytic ammonia synthesis. *Nat. Commun.* **15**, 6675 (2024).
22. Zhang, Z. et al. Graphdiyne Enabled Nitrogen Vacancy Formation in Copper Nitride for Efficient Ammonia Synthesis. *J. Am. Chem. Soc.* **146**, 14898-14904 (2024).
23. Feng, C. et al. Sub-Nanometer-Scale Cu_9S_5 Enables Efficiently Electrochemical Nitrate Reduction to Ammonia. *Adv. Energy Mater.* **15**, 2403354 (2025).
24. Huang, T. et al. Coordination environment-tailored electronic structure of single atomic copper sites for efficient electrochemical nitrate reduction toward ammonia. *Energy Environ. Sci.* **17**, 8360-8367 (2024).
25. Yang, W. et al. Triple Regulations via Fe Redox Boosting Nitrate Reduction to Ammonia at Industrial Current Densities. *Angew. Chem. Int. Ed.* **64**, e202415300 (2024).